

Article

Albedo-Induced Global Warming Impact at Multiple Temporal Scales within an Upper Midwest USA Watershed

Pietro Sciusco^{1,2,*}, Jiquan Chen^{1,2,3}, Vincenzo Giannico⁴, Michael Abraha^{2,3}, Cheyenne Lei^{1,2,3}, Gabriela Shirkey^{1,2}, Jing Yuan² and G. Philip Robertson^{3,5,6}

- ¹ Department of Geography, Environment & Spatial Sciences, Michigan State University, East Lansing, MI 48824, USA; jqchen@msu.edu (J.C.); cheyenne@msu.edu (C.L.); shirkeyg@msu.edu (G.S.)
² Center for Global Change and Earth Observations, Michigan State University, East Lansing, MI 48823, USA; abraha@msu.edu (M.A.); yuanji11@msu.edu (J.Y.)
³ Great Lakes Bioenergy Research Center, Michigan State University, East Lansing, MI 48824, USA; robert30@msu.edu
⁴ Department of Agricultural and Environmental Sciences, University of Bari A. Moro, 70126 Bari, Italy; vincenzo.giannico@uniba.it
⁵ W.K. Kellogg Biological Station, Michigan State University, Hickory Corners, MI 49060, USA
⁶ Department of Plant, Soil, and Microbial Sciences, Michigan State University, East Lansing, MI 48824, USA
* Correspondence: sciuscop@msu.edu; Tel.: +1-(517)-505-1074 or +39-(366)-3820032



Citation: Sciusco, P.; Chen, J.; Giannico, V.; Abraha, M.; Lei, C.; Shirkey, G.; Yuan, J.; Robertson, G.P. Albedo-Induced Global Warming Impact at Multiple Temporal Scales within an Upper Midwest USA Watershed. *Land* **2022**, *11*, 283. <https://doi.org/10.3390/land11020283>

Academic Editors: Javier Martínez-López, Alejandro Rescia, Robert Baldwin, Diane Pearson and Guillermo J. Martínez-Pastur

Received: 22 January 2022

Accepted: 8 February 2022

Published: 13 February 2022

Publisher's Note: MDPI stays neutral with regard to jurisdictional claims in published maps and institutional affiliations.



Copyright: © 2022 by the authors. Licensee MDPI, Basel, Switzerland. This article is an open access article distributed under the terms and conditions of the Creative Commons Attribution (CC BY) license (<https://creativecommons.org/licenses/by/4.0/>).

Abstract: Land surface albedo is a significant regulator of climate. Changes in land use worldwide have greatly reshaped landscapes in the recent decades. Deforestation, agricultural development, and urban expansion alter land surface albedo, each with unique influences on shortwave radiative forcing and global warming impact (GWI). Here, we characterize the changes in landscape albedo-induced GWI ($GWI_{\Delta\alpha}$) at multiple temporal scales, with a special focus on the seasonal and monthly $GWI_{\Delta\alpha}$ over a 19-year period for different land cover types in five ecoregions within a watershed in the upper Midwest USA. The results show that land cover changes from the original forest exhibited a net cooling effect, with contributions of annual $GWI_{\Delta\alpha}$ varying by cover type and ecoregion. Seasonal and monthly variations of the $GWI_{\Delta\alpha}$ showed unique trends over the 19-year period and contributed differently to the total $GWI_{\Delta\alpha}$. Cropland contributed most to cooling the local climate, with seasonal and monthly offsets of 18% and 83%, respectively, of the annual greenhouse gas emissions of maize fields in the same area. Urban areas exhibited both cooling and warming effects. Cropland and urban areas showed significantly different seasonal $GWI_{\Delta\alpha}$ at some ecoregions. The landscape composition of the five ecoregions could cause different net landscape $GWI_{\Delta\alpha}$.

Keywords: albedo; global warming impact (GWI); radiative forcing (RF); forest; land conversion; climate regulation; cooling effect; warming effect; landscape composition

1. Introduction

Surface albedo—the amount of solar radiation reflected by a surface relative to the total incident solar radiation—is a fundamental component of the Earth's surface energy balance [1,2]. Unlike greenhouse gases (GHGs), which regulate climate by the interception of longwave radiation that affects the Earth's radiation balance, the warming or cooling effects of surface albedo are directly due to instantaneous changes in the amounts of shortwave radiation reflected to outer space. Changes in land use worldwide have greatly reshaped landscapes in recent decades at increasing rates since the Industrial Revolution [3–6]. Earth's surface albedo has changed accordingly, resulting in alterations of the Earth's radiation balance that are partially responsible for the changing climate.

Globally, deforestation, agricultural development—including forest and grassland conversion—and urban expansion are major sources for albedo change [6,7], which, in turn, can directly affect the Earth's radiation balance. Imbalances due to albedo changes are

described by the albedo-induced radiative forcing ($RF_{\Delta\alpha}$, $W m^{-2}$)—changes in the fraction of solar radiation reflected back to the atmosphere from the Earth's surface [8]. For example, according to the Intergovernmental Panel on Climate Change (IPCC; [9]), the RF of well-mixed GHGs has a warming effect equivalent to $\sim+2.83 W m^{-2}$, while the $RF_{\Delta\alpha}$ due to land use and land cover change (LULCC) has a cooling effect equivalent to $\sim-0.15 W m^{-2}$. In other words, albedo changes have offset $\sim 5\%$ of the energy imbalance caused by well-mixed GHGs, with the offsets varying substantially by region. However, this offset is a global average in reference to LULCC, with dominant changes from forest to non-forest since 1750. Therefore, the local contributions of $RF_{\Delta\alpha}$ due to LULCC are unknown and might play an important role in the overall global average of climate regulation effects.

The present scientific understanding of the forcing effects of albedo due to LULCC is ranked as medium-low relative to the rich scientific evidence of the forcing effects of GHGs [1]. To cross-examine effects with the climate impact of other GHGs (i.e., biogeochemical GWI), albedo-induced warming or cooling can be converted into equivalents of carbon-dioxide (CO_{2eq}) and/or carbon (C_{eq}) atmospheric radiative forcing via the concept of albedo-induced global warming potential ($GWP_{\Delta\alpha}$, $kg CO_{2eq} m^{-2} yr^{-1}$; [9,10]) metric—hereinafter referred to as global warming impact ($GWI_{\Delta\alpha}$), to be in line with our previous study [11]. For example, Houspanossian et al. [12] found that conversion from forests to croplands, from forests to pastures, and from pastures to croplands in dry subtropical forests of South America offset $12\text{--}27 Mg C_{eq} ha^{-1}$ during a 12-year period, or from 15% to 55% of the total C emissions due to deforestation. In Europe, Carrer et al. [13] reported that inclusion of cover crops in annual cropping systems could have cooling effects equivalent to a mitigation of $-0.03 Mg C_{eq} ha^{-1} yr^{-1}$, while Lugato et al. [14] showed that such mitigation potential due to the inclusion of cover crops could be substantially enhanced by growing high-albedo chlorophyll-deficient cover crops. In southwest Michigan, USA, Chen et al. [15] estimated that land conversion from forest to maize (*Zea mays* L.) can provide a cooling equivalent to a mitigation of $-0.043 Mg C_{eq} ha^{-1} yr^{-1}$ due to a 0.051 (i.e., 5.1%) increase in albedo. At watershed scale, Sciusco et al. [11] demonstrated that altered landscapes could produce cooling effects relative to the intact, native, late successional forests typical of pre-European settlement and contribute a range of -0.1 to $-0.4 Mg C_{eq} ha^{-1} yr^{-1}$, which is the same order of magnitude of biogeochemical GWI emissions due to many crop management components [16,17].

Despite the potential importance of albedo modification strategies for regional to global climate mitigation by IPCC [18] and numerous discussions [19,20] on intentionally increasing surface albedo to cool the Earth, little effort has been made to understand changes in landscape $RF_{\Delta\alpha}$ or $GWI_{\Delta\alpha}$ in the context of landscape composition at broader temporal scales and for multiple anthropogenic LULCC [11,21,22]. A critical unknown is how different cover types contribute to total landscape $GWI_{\Delta\alpha}$ at different times of the year. Over the long term (i.e., years to decades), little is known about whether the intra-annual variations of landscape $GWI_{\Delta\alpha}$ are significant.

Here, we build on Sciusco et al. [11] to estimate the contributions of the $GWI_{\Delta\alpha}$ to the landscape warming or cooling effects at seasonal and monthly timescales over 19 years for multiple ecoregion subtypes. We quantify different cover types in different ecoregions of the upper Midwest USA watershed by estimating (1) the monthly and seasonal contributions to the total landscape cooling or warming; (2) the variations of $GWI_{\Delta\alpha}$ contributions by cover type, ecoregion, and year; and (3) the magnitude of cooling or warming effects due to land cover change relative to mature forest cover.

2. Materials and Methods

2.1. Study Area and Landscape Composition

The Kalamazoo River Watershed (5621 km²; Figure 1) is located in southwest Michigan, USA, and includes portions of 10 counties: Allegan, Barry, Calhoun, Eaton, Hillsdale, Jackson, Kalamazoo, Kent, Ottawa, and Van Buren. The mean annual temperature (1981–2010) is 9.9 °C, and the average annual precipitation is 900 mm evenly distributed throughout

the year [23]. The dominant cover type prior to European settlement in the early 1800s was eastern broadleaf deciduous forest [24], with scattered patches of tallgrass prairie, oak savanna, lakes, and wetlands [25]. The dominant land cover includes cultivated crops, successional forest stands, pasture-hay grasslands, and two urban areas (i.e., Kalamazoo and Battle Creek). Medium to coarse texture soils and mesic climate allow the continuous recharge of groundwater [26].

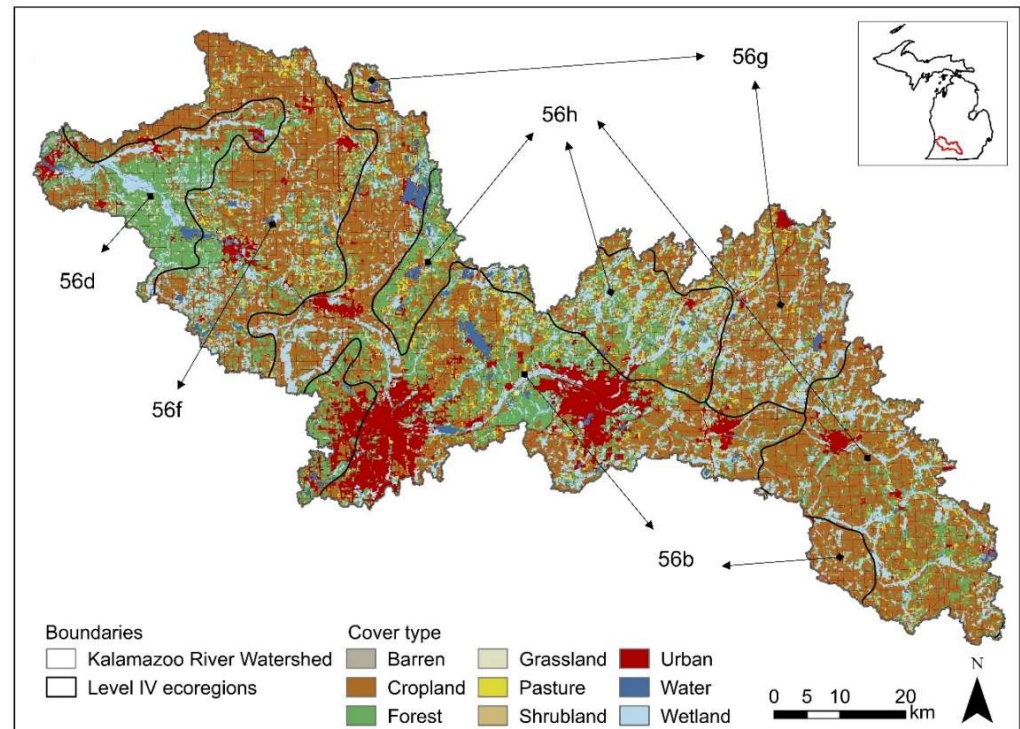


Figure 1. The study area of the five United States Environmental Protection Agency Level IV ecoregions and the nine National Land Cover Database cover type classes within the Kalamazoo River Watershed in 2001. (Map projection: WGS-84 UTM Zone 16 N).

Within the watershed, there are five United States Environmental Protection Agency (US EPA) Level IV ecoregions (Figure 1). Level IV ecoregions have the finest resolution and exhibit unique physiographic, geologic, pedologic, botanic, hydrologic, and climatic characteristics [27]. The five ecoregions studied here are Battle Creek Outwash Plain (56b), Michigan Lake Plain (56d), Lake Michigan Moraines (56f), Lansing Loamy Plain (56g), and Interlobate Dead Ice Moraines (56h). For further details, see the US EPA [28].

In this study, we used the National Land Cover Database (NLCD; [29,30]), which provides nine land cover types (barren, cropland, forest, grassland, pasture, shrubland, urban, water, and wetland) at 30×30 m spatial resolution, with an overall accuracy ranging between 80% and 90%, in the central and western U.S. [29]. Land cover classifications from NLCD are available for the years 2001, 2004, 2006, 2008, 2011, 2013, and 2016. Because land cover maps from NLCD are not annually provided like albedo data (see next section), we assumed land cover is similar to the prior year for years where NLCD data are not available. For example, the land cover map for 2002 was assumed to be the same as that of 2001, and for 2017–2019, we assumed the land cover had no significant changes.

2.2. Intra-Annual Changes in Albedo

We obtained instantaneous albedo data at 10:30 a.m. local time (MODIS Terra morning overpassing time) at 500×500 m spatial resolution and at daily time-step for 2001–2019 from the most recent collection (V006) of the MODIS Bidirectional Reflectance Distribution Function (BRDF) MCD43A3 product [31]. The MCD43A3 product contains both black-sky

(i.e., directional-hemispherical reflectance) and white-sky (i.e., bi-hemispherical reflectance) albedos [32]. We considered white-sky albedo (α) at a shortwave length of 0.3–5.0 μm by growing season and month during 2001–2019.

Growing season and monthly albedos (α_{gs} and α_{mo} , respectively) at 10:30 a.m. local time were derived by stacking (i.e., median image composite) the daily images into growing seasons or months by year. Specifically, α_{gs} accounted for 19 composites (2001–2019), while α_{mo} accounted for 11 composites (January–December, over the 19-year period, less March, which we removed because few images were available and likely due to high cloud cover). We applied the same methodology as Jeong et al. [33] and Sciusco et al. [11] to identify the growing season (roughly from March to November) for each year. Briefly, we used the enhanced vegetation index (EVI; see Appendix A) to identify the growing season by detecting the EVI inflection points (i.e., the dates) when maximum and minimum change rate in greenness occurred over the entire watershed (which was roughly between March and November for the 19-year period).

We employed the Google Earth Engine platform [34] to analyze and process all datasets (see Appendix A). We then performed a zonal statistical analysis within ArcMap (v. 10.6) to calculate the proportion of NLCD cover types within each MODIS pixel, and to extract α_{gs} and α_{mo} values by pixel before statistical analysis in RStudio v.1.2.5033 [35].

2.3. Albedo-Induced Global Warming Impact ($\text{GWI}_{\Delta\alpha}$)

We employed the linear downscaling approach of Chen et al. [36] to estimate surface albedo of cover type i ($\hat{\alpha}_{si}$) at each MODIS pixel. For a MODIS pixel, $\hat{\alpha}_{si}$ is considered as the sum of surface albedo of cover type i (α_{si}) within each MODIS pixel, as follows [36]:

$$\hat{\alpha}_{si}(t) = \left[\sum (k_i \times \alpha_{si}(t)) \right] + \varepsilon_t \quad (1)$$

where $\hat{\alpha}_{si}$ is the estimated surface albedo of cover type i for a time-period (t) (i.e., GS: $t = 2001$ – 2019 and monthly: $t = \text{January}$ – December , less March), k_i is the proportion (0–1) of cover type i in each MODIS pixel, and ε_t represents model residuals.

The calculation of landscape albedo-induced radiative forcing ($\text{RF}_{\Delta\alpha}$) and global warming impact ($\text{GWI}_{\Delta\alpha}$) is based on the change in surface albedo due to land cover conversion. This is normally considered as the surface albedo difference ($\Delta\alpha_s$) between a cover type i and the native vegetation cover type (i.e., the reference) [11]. Here, forest is the dominant land cover type prior to European settlement and serves as our reference [24]. Thus, the surface albedo difference of cover type i ($\Delta\alpha_{si}$) for growing season and monthly periods and for each ecoregion at 10:30 a.m. local time is calculated as:

$$\Delta\alpha_{si} = (\hat{\alpha}_{si} - \hat{\alpha}_{sf}) \quad (2)$$

where $\hat{\alpha}_{si}$ and $\hat{\alpha}_{sf}$ are the estimated surface albedos of cover type i and of the reference forest f for growing season and monthly periods and for each ecoregion. We calculated $\Delta\alpha_{si}$ only when the proportion of a cover type i was $\geq 80\%$ of the 500×500 m MODIS pixel. Conversions to barren, grassland, and shrubland were excluded, as they have a small percentage of the total study area, as were current water and wetland covers. Consequently, only cropland, forest, pasture, and urban covers were considered in this study.

We then used $\Delta\alpha_{si}$ to calculate the landscape $\text{RF}_{\Delta\alpha}$ as follows [13,37,38]:

$$\text{RF}_{\Delta\alpha} = -(SW_{in} \cdot K_T \cdot \Delta\alpha_{si}) \quad (3)$$

where $\text{RF}_{\Delta\alpha}$ (W m^{-2}) is the landscape albedo-induced radiative forcing at the top-of-atmosphere at 10:30 a.m. local time, and SW_{in} , K_T , and $\Delta\alpha_{si}$ are the incident shortwave radiation at the surface, the clearness index (for more details, see Equations (A1)–(A5) in Appendix A), and the surface albedo difference between a cover type i and the reference forest, respectively, for the growing season and monthly periods and for each ecoregion (Equation (2)). The incident shortwave radiation at the surface (SW_{in}) and the clearness

index (K_T) were derived from the solar and meteorological dataset NASA POWER [39] at daily time-step for multiple locations (i.e., five Level IV ecoregions) within the Kalamazoo River Watershed. We then averaged SW_{in} and K_T values to match the 19 growing seasons and the 11 months. Positive or negative values of $RF_{\Delta\alpha}$ indicate warming and cooling effects, respectively.

Lastly, we calculated the landscape $GWI_{\Delta\alpha}$ as follows [13,37,38]:

$$GWI_{\Delta\alpha} = \left(\frac{A \cdot RF_{\Delta\alpha}}{AF(t) \cdot rf_{CO_2}} \cdot \frac{1}{TH} \right) \quad (4)$$

where $GWI_{\Delta\alpha}$ ($\text{kg CO}_{2\text{eq}} \text{m}^{-2} \text{yr}^{-1}$) is the landscape albedo-induced global warming impact for the growing season and monthly periods in each ecoregion at 10:30 a.m. local time, A is the area for which the hypothesized albedo change occurred (here normalized to 1m^2), $AF(t)$ is the CO_2 airborne fraction that remains in the atmosphere at time (t) following a single pulse emission, rf_{CO_2} is the marginal RF for CO_2 emissions at a given atmospheric concentration, and TH represents the time horizon of global warming. The parameter $AF(t)$ is modeled with an exponential function through a multi-model impulse response function analysis (for more details, see Equation (A6) in Appendix A) [40], while rf_{CO_2} is kept constant at $0.908 \text{W kg CO}_2^{-1}$ [13,41,42] and TH is fixed at 100 years (i.e., the number of time steps the GWI is then divided by) [43,44]. With Equation (4), we calculate the equivalent $RF_{\Delta\alpha}$ that a unit area of A would have at the global scale. Positive or negative values of the $GWI_{\Delta\alpha}$ indicate effects equivalent to CO_2 emission or mitigation, respectively. Here, we report the results of landscape seasonal and monthly $GWI_{\Delta\alpha}$ ($GWI_{\Delta\alpha\text{gs}}$ and $GWI_{\Delta\alpha\text{mo}}$, respectively) expressed with units of $\text{Mg C}_{\text{eq}} \text{ha}^{-1} \text{gs}^{-1}$ and $\text{Mg C}_{\text{eq}} \text{ha}^{-1} \text{mo}^{-1}$, respectively, which refer to 10:30 a.m. local time.

2.4. Contributions of Land Cover Change to $GWI_{\Delta\alpha}$

We performed a nested analysis of variance (ANOVA) with repeated measurements (i.e., growing season and monthly periods) to quantify the contribution to landscape $GWI_{\Delta\alpha}$ by cover type and ecoregion for the growing season and monthly periods. Specifically, we looked at contributions among and within the five ecoregions, with two linear models:

$$GWI_{\Delta\alpha}(t) = (\text{ecoregion} \times \text{cover type})(t) \quad (5)$$

$$GWI_{\Delta\alpha}(t) = \text{cover type}(t) \quad (6)$$

where *ecoregion* refers to the five Level IV ecoregions (i.e., 56b, 56d, 56f, 56g, and 56h), and *cover type* refers to the three cover types (i.e., cropland, pasture, and urban) used to determine the albedo difference from the reference forest (Equation (2)) for growing season and monthly periods at each ecoregion. For further details about the ANOVA analysis, see Appendix A.

3. Results

3.1. Land Use and Land Cover Change

The dominant land cover types in the Kalamazoo River Watershed—cropland, forest, pasture, and urban cover—underwent detectable changes during 2001–2016 (Table 1). Declines were the highest for forest (1500 ha, -1.3%), followed by pasture (1087 ha, -3.83%) and cropland (714 ha, -0.33%).

Gains occurred for urban cover type (~ 2000 ha, $\sim +3\%$). Cropland, forest, and pasture were converted into a variety of cover types (Table 2): Cropland was primarily converted into urban (1157 ha), pasture (776 ha), and forest (137 ha), forest was largely converted into urban (515 ha) and cropland (164 ha), while pasture was mostly converted into cropland (1456 ha) and urban (197 ha).

Table 1. Land cover composition in ha (%) of the Kalamazoo River Watershed, and net gain (+) and loss (−) for each cover type during the period 2001–2016.

Cover Type	Land Cover Composition		Land Cover Gain (+) or Loss (−)
	ha (%)		
	2001	2016	2001–2016
Cropland	215,869 (40.90)	215,155 (40.80)	−714 (−0.33)
Forest	115,393 (21.90)	113,893 (21.60)	−1500 (−1.30)
Pasture	28,382 (5.40)	27,296 (5.20)	−1087 (−3.83)
Urban	66,759 (12.70)	68,743 (13.00)	+1984 (+2.89)

Table 2. Pivot table showing the land cover conversion (ha) of each cover type during the period 2001–2016 across the Kalamazoo River Watershed. Bold values indicate the main land cover conversions, while “*” indicates no land cover conversion.

		Land Cover Conversion (ha) 2001–2016				
2001 \ 2016		Cropland	Forest	Pasture	Urban	Total ₂₀₀₁
Cropland		212,802 *	137	776	1157	214,872
Forest		164	113,337 *	9	515	114,025
Pasture		1456	57	26,467 *	197	28,176
Urban		16	21	8	66,704 *	66,748
Total ₂₀₁₆		21,4437	113,552	27,259	68,573	423,821

3.2. Albedo and $GWI_{\Delta\alpha}$ in Time and Space

The linear downscaling model (Equation (1)) showed that each cover type contributed differently to the total α_{gs} (adj. $R^2 = 0.995$) and α_{mo} (adj. $R^2 = 0.745$) (Table S1). The four cover types had an overall average α_{gs} of 0.16 ± 0.013 (Table S2), with cropland having the highest α_{gs} at 0.17 ± 0.002 (Table S2), followed closely by pasture (0.16 ± 0.003), urban (0.15 ± 0.002), and forest (0.15 ± 0.004) covers. On the other hand, the α_{mo} (overall average: 0.23 ± 0.134) had a higher variation than α_{gs} and was higher in January, February, and December, with a maximum of 0.46 ± 0.109 in February (Table S2). Other months exhibited lower α_{mo} , with a minimum of 0.14 ± 0.017 in November. Cropland and pasture had the highest α_{mo} (0.28 ± 0.183 and 0.25 ± 0.156 , respectively). However, the remaining cover types ranked differently for α_{mo} than for α_{gs} , decreasing in the order urban (0.22 ± 0.119) and forest (0.19 ± 0.080). As with α , $\Delta\alpha$ varied substantially across cover types but was relatively constant within a cover type among the ecoregions (Figure 2a,b). In particular, $\Delta\alpha_{gs}$ ranged from -0.001 ± 0.003 for urban to 0.026 ± 0.004 for cropland cover (Figure 2a), while $\Delta\alpha_{mo}$ had higher variation and ranged from 0.024 ± 0.040 for urban to 0.089 ± 0.108 for cropland cover (Figure 2b).

The average $GWI_{\Delta\alpha}$ showed an overall cooling effect (Figure 3a,b) for most cover types, with the exception of urban, which showed neutral effects. Overall, cropland cover type had seasonal and monthly average cooling effects equivalent to $-0.35 \pm 0.05 \text{ Mg C}_{eq} \text{ ha}^{-1} \text{ gs}^{-1}$ and $-0.68 \pm 0.61 \text{ Mg C}_{eq} \text{ ha}^{-1} \text{ mo}^{-1}$, respectively (Figure 3a,b). The highest seasonal and monthly cooling effects reached $-0.47 \text{ Mg C}_{eq} \text{ ha}^{-1} \text{ gs}^{-1}$ (in 2015 for Ecoregions 56b, 56d, 56f, and 56h; Tables S3.1–3.3, and 3.5 and $-2.15 \text{ Mg C}_{eq} \text{ ha}^{-1} \text{ mo}^{-1}$ (in February for Ecoregion 56b; Table S4.1), for the two periods, respectively. These cooling effects represented ~26% and ~68% more than the seasonal and monthly annual averages, respectively. On the other hand, urban cover was the only cover type showing neutral effects (i.e., seasonal and monthly average effects equivalent to $-0.001 \pm 0.034 \text{ Mg C}_{eq} \text{ ha}^{-1} \text{ gs}^{-1}$ and $-0.158 \pm 0.256 \text{ Mg C}_{eq} \text{ ha}^{-1} \text{ mo}^{-1}$, respectively; Figure 3a,b).

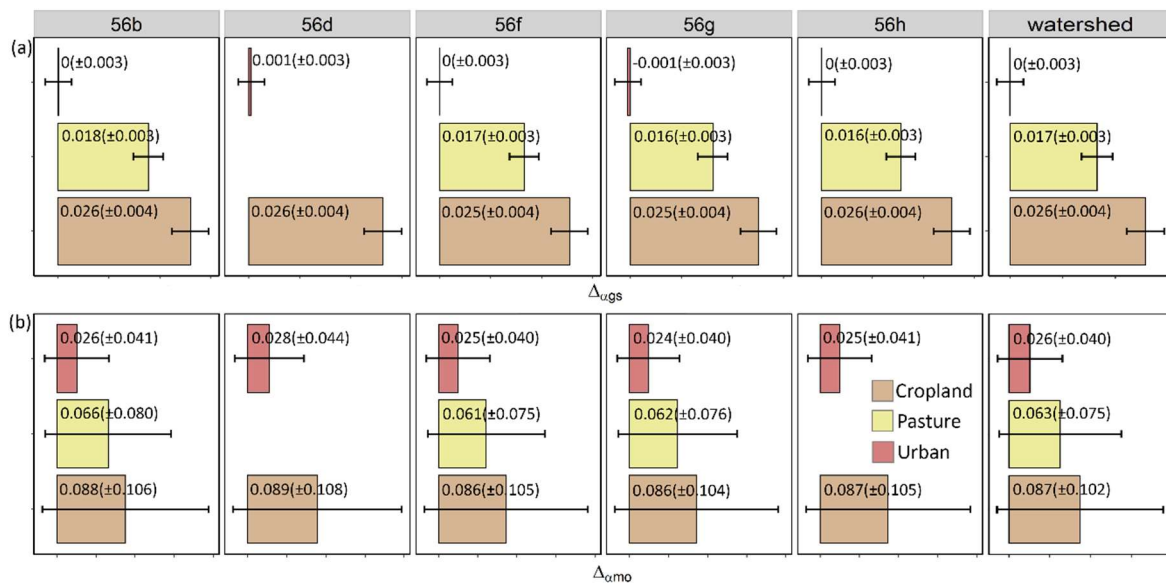


Figure 2. Albedo difference ($\Delta\alpha$) between a cover type *i* and the forest for (a) growing season ($\Delta\alpha_{gs}$) and (b) monthly ($\Delta\alpha_{mo}$) periods, within the five Level IV ecoregions and the entire Kalamazoo River Watershed 2001–2019. Annotations indicate mean (\pm standard deviation) of $\Delta\alpha_{gs}$ and $\Delta\alpha_{mo}$.

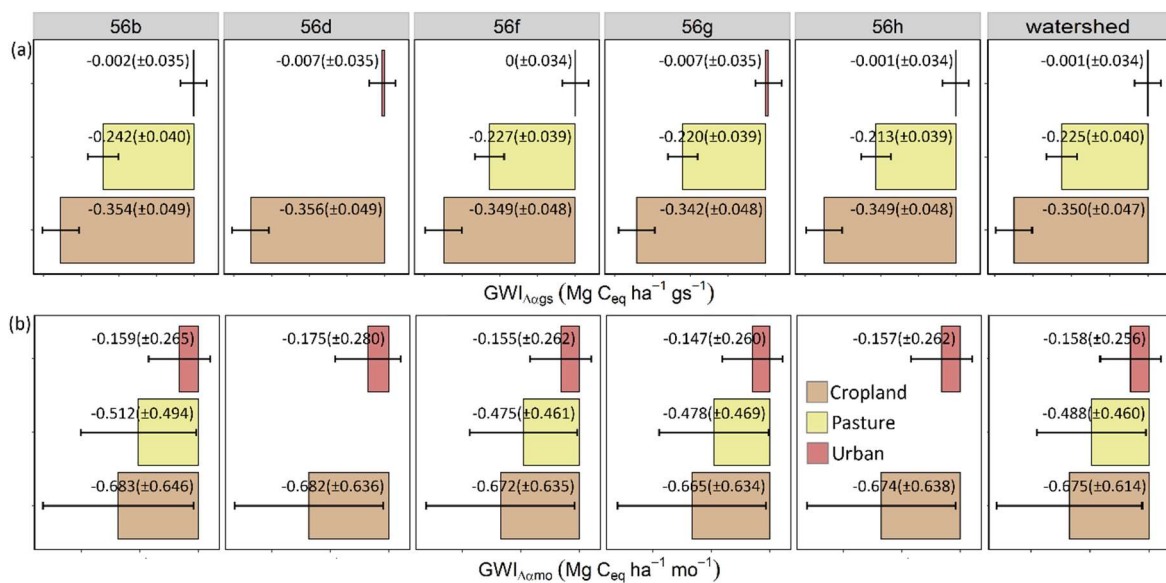


Figure 3. Albedo-induced global warming impact ($GWI_{\Delta\alpha}$) for (a) growing season ($GWI_{\Delta\alpha_{gs}}$) and (b) monthly ($GWI_{\Delta\alpha_{mo}}$) periods, within the five Level IV ecoregions and the entire Kalamazoo River Watershed 2001–2019. Annotations indicate mean (\pm standard deviation) of $GWI_{\Delta\alpha_{gs}}$ and $GWI_{\Delta\alpha_{mo}}$.

All three cover types showed similar trends in $GWI_{\Delta\alpha_{gs}}$ 2001–2019 across the five ecoregions (Tables S3.1–3.5 and Figure 4a) with similar deviations from the $GWI_{\Delta\alpha_{gs}}$ mean. The growing season cooling effects ($GWI_{\Delta\alpha_{gs}}$) ranged between -0.39 and -0.47 $Mg\ C_{eq}\ ha^{-1}\ gs^{-1}$ for cropland, between -0.25 and -0.31 $Mg\ C_{eq}\ ha^{-1}\ gs^{-1}$ for pasture, and between -0.01 and -0.11 $Mg\ C_{eq}\ ha^{-1}\ gs^{-1}$ for urban. Urban was the only cover type that also showed warming effects, with $GWI_{\Delta\alpha_{gs}}$ ranging between 0.01 and 0.05 $Mg\ C_{eq}\ ha^{-1}\ gs^{-1}$. The inter-monthly variation of $GWI_{\Delta\alpha_{mo}}$ for cropland, pasture, and urban cover showed similar trends with higher cooling effects in January, February, and December (Tables S4.1–4.5 and Figure 4b). Among the three cover types, the highest cooling occurred in cropland (-0.18 to -2.15 $Mg\ C_{eq}\ ha^{-1}\ mo^{-1}$), followed by pasture (-0.13 to -1.64 $Mg\ C_{eq}\ ha^{-1}\ mo^{-1}$) and urban (-0.02 to -0.470 $Mg\ C_{eq}\ ha^{-1}\ mo^{-1}$) cover. For the

three cover types, $\text{GWI}_{\Delta\alpha\text{mo}}$ was relatively constant from April to November. However, urban had slightly bell-shaped trends with small warming effects in June and July (0.01 to $0.1 \text{ Mg C}_{\text{eq}} \text{ ha}^{-1} \text{ mo}^{-1}$; Tables S4.1–4.5 and Figure 4b), and cropland had an inverted bell-shaped trend with slight rises in June and October. Lastly, pasture (in Ecoregions 56b, 56f, and 56g) had relatively constant trends. The variation among ecoregions in $\text{GWI}_{\Delta\alpha\text{gs}}$ was significant ($p < 0.001$) by ecoregion, cover type, and their interactions (ANOVA model in Equation (5); Table S5), while the variation in $\text{GWI}_{\Delta\alpha\text{mo}}$ was significant ($p < 0.001$) only by cover type. Neither years nor months were significant for $\text{GWI}_{\Delta\alpha}$ variations. Most of the variation in $\text{GWI}_{\Delta\alpha\text{gs}}$ was explained by cover type ($\eta^2 = \sim 95\%$), followed by the interaction between ecoregions and cover type ($\eta^2 = \sim 52\%$) and ecoregions ($\eta^2 = 32\%$). In comparison, the variation in $\text{GWI}_{\Delta\alpha\text{mo}}$ was almost equally explained by ecoregion, cover type, and their interactions, although only cover type was significant ($\eta^2 = \sim 24\%$ at $p < 0.001$). The variation in both $\text{GWI}_{\Delta\alpha\text{gs}}$ and $\text{GWI}_{\Delta\alpha\text{mo}}$ within ecoregions (Equation (6); Table S5), however, was significant ($p < 0.001$) by cover type, which explained more of the variation in $\text{GWI}_{\Delta\alpha\text{gs}}$ ($\eta^2 = 99\%$) than in $\text{GWI}_{\Delta\alpha\text{mo}}$ ($\eta^2 = 65\%$).

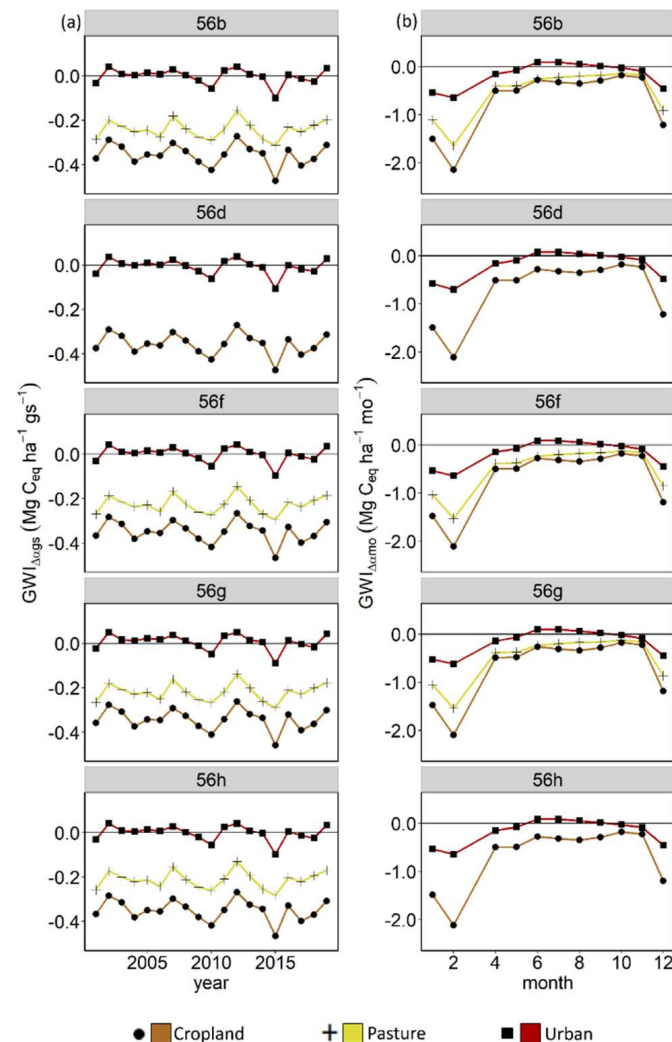


Figure 4. Albedo-induced global warming impact ($\text{GWI}_{\Delta\alpha}$) for a given cover type within the five Level IV ecoregions. Panels (a,b) represent the $\text{GWI}_{\Delta\alpha}$ for the growing season ($\text{GWI}_{\Delta\alpha\text{gs}}$; 2001–2019) and monthly ($\text{GWI}_{\Delta\alpha\text{mo}}$; January–December, less March) periods, respectively. Positive and negative values of $\text{GWI}_{\Delta\alpha}$ indicate warming and cooling effects, respectively, equivalent to Carbon (C_{eq}) emission and mitigation, respectively.

A post-hoc Tukey test analysis (Figure 5a,b) showed that, within each ecoregion, the least square means (LSMs) of $\text{GWI}_{\Delta\alpha_{\text{GS}}}$ had low variability and were significantly different among the cover types (Figure 5a). The LSMs for $\text{GWI}_{\Delta\alpha_{\text{mo}}}$ were more variable, and many cover types had statistically similar means (Figure 5b). Among ecoregions, the LSMs of cropland $\text{GWI}_{\Delta\alpha_{\text{GS}}}$ at Ecoregion 56g were significantly different from those at Ecoregions 56b and 56d, while the LSMs at urban $\text{GWI}_{\Delta\alpha_{\text{GS}}}$ at Ecoregion 56g were significantly different from those at Ecoregion 56d. However, no significant differences in their LSMs for $\text{GWI}_{\Delta\alpha_{\text{mo}}}$ were observed (Figure 5b).

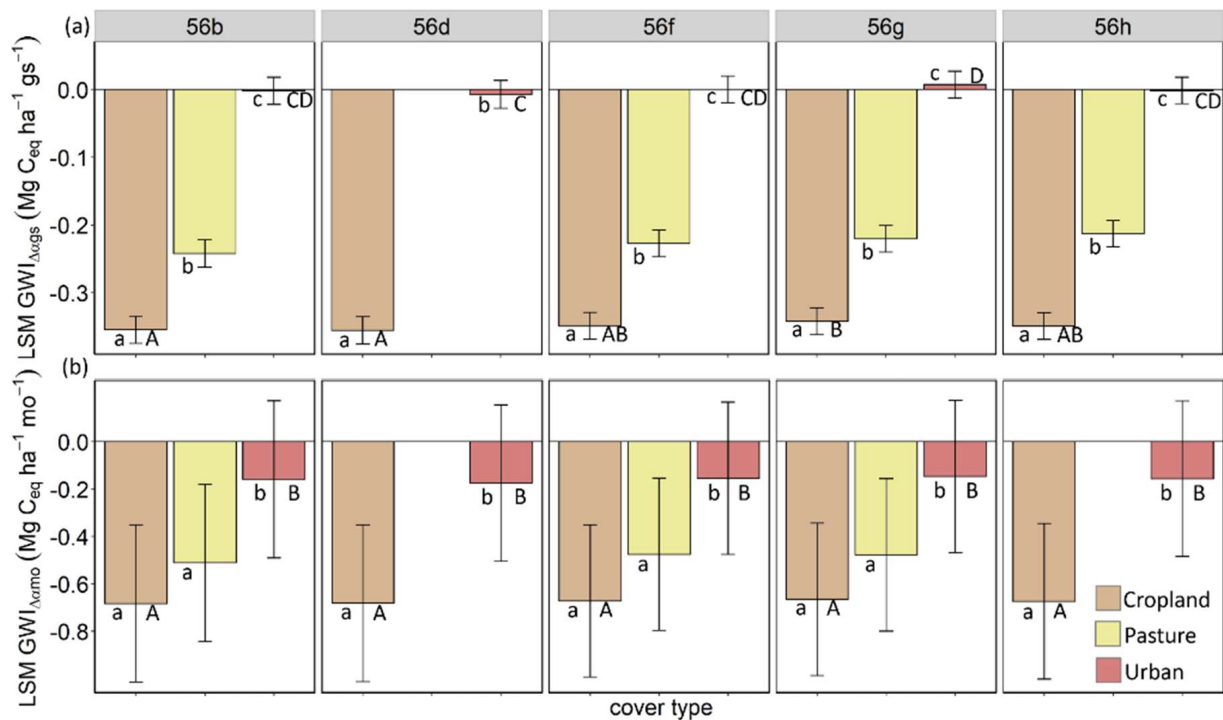


Figure 5. The least square means (LSMs) multi-comparison analysis of albedo-induced global warming impact ($\text{GWI}_{\Delta\alpha}$) for a given cover type across the five Level IV ecoregions for the (a) growing season ($\text{GWI}_{\Delta\alpha_{\text{GS}}}$; 2001–2019) and (b) monthly ($\text{GWI}_{\Delta\alpha_{\text{mo}}}$; January–December) periods. Whiskers represent the lower and upper limits of the 95% family-wise confidence level of the LSMs. Bars sharing the same letters are not significantly different according to the post-hoc Tukey test analysis. Lowercase letters indicate differences among cover types within the five ecoregions, while uppercase letters indicate differences of same cover type among the five ecoregions. The among ecoregions analysis only considered cropland and urban covers (i.e., the cover types that were in every ecoregion).

The overall $\text{GWI}_{\Delta\alpha}$ contribution from different seasons and months varied by cover type, and it was exclusively higher during the non-growing season (NGS) than during the growing season (GS) months for all ecoregions (Table S6 and Figure 6), with the NGS months being characterized by only cooling effects (Table S7). As a general trend, the highest contributions were in February and the lowest in October. During the NGS, urban (at all ecoregions) contributed the most to the total cooling effect (between 18% and 31%), followed by pasture (at Ecoregions 56b, 56f, and 56g; contribution between 14% and 25%), and cropland (at all ecoregions; contribution between 14% and 24%). It is worth noting that during GS months, no cover type had a contribution $>8\%$ (i.e., 1/12 of the annual total). Nevertheless, climate regulations of urban (for all ecoregions) were close to the overall mean value of 8% in April, while cropland (at all ecoregions) and pasture (at Ecoregions 56b, 56f, and 56g) were close in April and May.

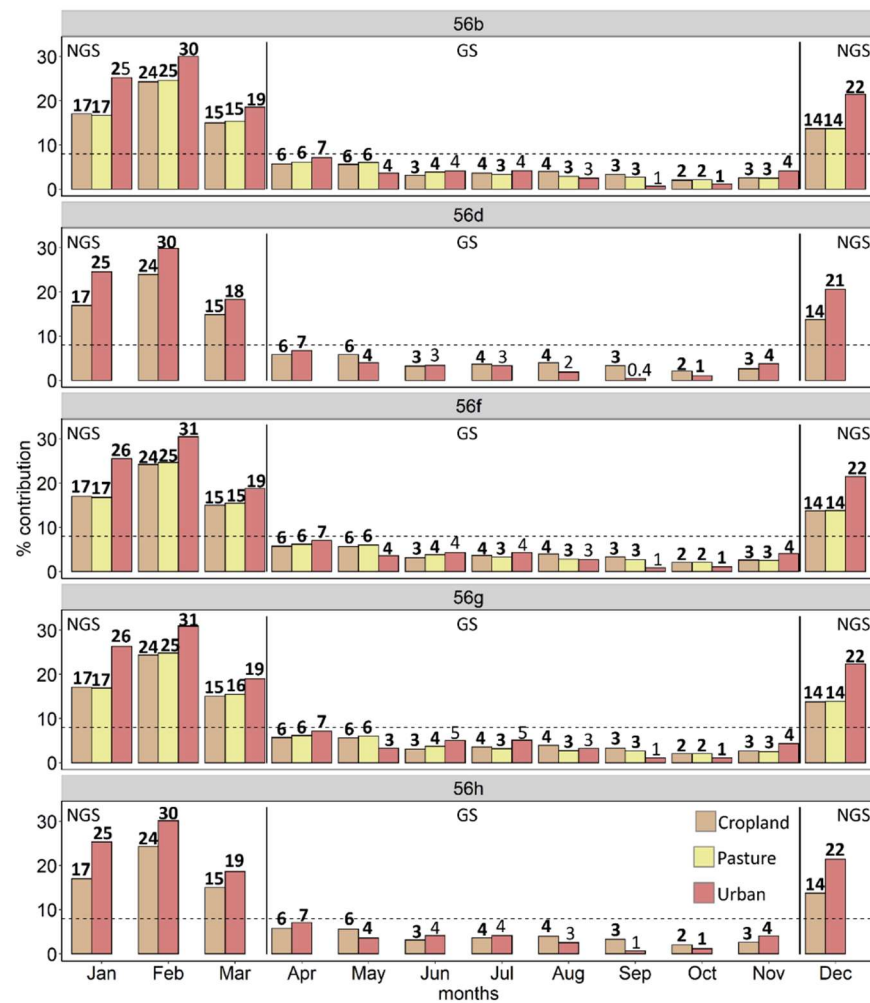


Figure 6. Percent contribution of albedo-induced global warming impact ($GWI_{\Delta\alpha}$) to cooling (values in bold) or warming effects by season and month periods for major cover types in the five Level IV ecoregions. The horizontal dashed line represents the average contribution $\sim 8\%$ (i.e., 1/12 of the annual total), and the solid vertical lines separate the non-growing season (NGS) from the growing season (GS) months. Values of March were missing and gap-filled as the mean $GWI_{\Delta\alpha}$ of February and April.

4. Discussion

Our results showed that the albedo-induced global warming impact ($GWI_{\Delta\alpha}$) accounted for a significant portion of the climate cooling effects (i.e., C_{eq} mitigation) due to land cover changes and landscape composition. Individual contributions varied by cover type, ecoregion, and season/month, with cropland showing the highest cooling effects, followed by pasture. Urban showed both cooling and warming effects, the latter of which occurred only during growing season months. Overall, the cooling effects of the monthly $GWI_{\Delta\alpha}$ were higher than the seasonal ones, most likely due to the substantial influence of snow cover on land surface albedo (i.e., high presence of snow during the winter months; [45]) combined with the effect of management practices on different vegetation surfaces. For example, snowfalls on harvested crop fields create a highly reflective layer, whereas on forested fields, snowfalls tend to be masked by the tree structures and reflect less. For the same reason, seasonal analysis showed that the cooling contributions during the non-growing season months were higher than during the growing season months. Overall, our results seem to be promising in the context of climate regulation of albedo changes due to land cover changes and landscape composition. Nevertheless, several assumptions and limitations to our study could benefit GWI computations elsewhere.

4.1. Cooling Effects

During the 19-year study period, the highest cropland cooling effect of the seasonal and monthly $\text{GWI}_{\Delta\alpha}$ was equivalent to $-0.47 \text{ Mg C}_{\text{eq}} \text{ ha}^{-1} \text{ gs}^{-1}$ in 2015 for Ecoregions 56b, 56d, 56f, and 56h, and $-2.15 \text{ Mg C}_{\text{eq}} \text{ ha}^{-1} \text{ mo}^{-1}$ in February for Ecoregion 56b, respectively. In comparison, Abraha et al. [46], accounting for GHGs using whole-system lifecycle analysis, found emissions of $2.6 \text{ Mg C}_{\text{eq}} \text{ ha}^{-1} \text{ yr}^{-1}$ over 8 years in Conservation Reserve Program (CRP) grasslands converted to maize. Thus, the seasonal and monthly maximum albedo-induced cooling effects from cropland represent (i.e., offset) 18% and ~83%, respectively, of the annual C_{eq} over the 8 years from CRP grasslands converted to maize fields. The total highest albedo cooling effect due to both the seasonal and monthly $\text{GWI}_{\Delta\alpha}$ would completely offset the annual emissions due to the grassland converted to maize over the 8 years. Moreover, the abovementioned cropland cooling effects are more than enough to offset the annual net biogeochemical GWI —i.e., warming effects due to the net contributions from CO_2 , methane (CH_4), and nitrous-oxide (N_2O) at $0.31 \text{ Mg C}_{\text{eq}} \text{ ha}^{-1} \text{ yr}^{-1}$ —produced by annual crop systems (i.e., maize-soybean-wheat rotation) under conventional tillage management of the same area [47].

4.2. Variable Effects

Urban areas appeared to have either cooling or warming effects depending on the temporal scale examined. Unlike cropland, which had cooling effects during summer months mostly due to changes in vegetation over the growing season [48–52], urban cover had warming effects over the growing season months and cooling effects during the rest of the year. At Ecoregion 56g, the highest seasonal and monthly warming effects, estimated at $0.05 \text{ Mg C}_{\text{eq}} \text{ ha}^{-1} \text{ gs}^{-1}$ in 2002 and 2012, and $\sim 0.1 \text{ Mg C}_{\text{eq}} \text{ ha}^{-1} \text{ mo}^{-1}$ in June and July, are equivalent to ~29% and 45%, respectively, of the annual net ecosystem production (NEP) of deciduous forest stands in northern Michigan [53]. On the other hand, the maximum monthly cooling effect of urban landscapes at Ecoregion 56h was equivalent to $-0.7 \text{ Mg C}_{\text{eq}} \text{ ha}^{-1} \text{ mo}^{-1}$ (in February). In comparison, Xu et al. [38] estimated a C_{eq} offset between $-2.2 \text{ Mg C}_{\text{eq}} \text{ ha}^{-1}$ and $-4.4 \text{ Mg C}_{\text{eq}} \text{ ha}^{-1}$ induced by an increase in pavement albedo of 0.01 (i.e., 1%) across two major US cities over a 50-year period. Such results are important, considering that the watershed includes two major urban centers, Kalamazoo and Battle Creek, with a total population of >500,000 people in 2010 [36]. More so, as previous studies predicted [54], Michigan urban areas is anticipated to increase >50% by 2030.

4.3. Intra- and Inter-Annual Variability of Albedo and $\text{GWI}_{\Delta\alpha}$

Despite our expectation that the intra- and inter-annual variability of surface albedo would vary due to seasonality and climatic conditions [11], we did not find significant differences in inter-annual variation of $\Delta\alpha$ nor $\text{GWI}_{\Delta\alpha}$. For example, each cover type showed unique inter-annual trends that appeared to be similar during the seasonal and monthly periods. However, we found that during the growing season, the $\text{GWI}_{\Delta\alpha}$ of cropland and urban cover types was not the same in every ecoregion, which emphasizes that cover types may have different contributions depending on the location. In other words, changes in landscape composition in the five ecoregions could cause different net landscape $\text{GWI}_{\Delta\alpha}$. For example, contrasting landscape compositions among the five ecoregions led to different cumulative cooling effects during the growing season over 19 years. This value varied from $-6.89 \text{ Mg C}_{\text{eq}} \text{ ha}^{-1} \text{ gs}^{-1}$ to $-11.36 \text{ Mg C}_{\text{eq}} \text{ ha}^{-1} \text{ gs}^{-1}$ at Ecoregions 56d and 56b, respectively. At monthly scales, landscape composition produced cumulative cooling effects between $-9.14 \text{ Mg C}_{\text{eq}} \text{ ha}^{-1} \text{ mo}^{-1}$ and $-14.89 \text{ Mg C}_{\text{eq}} \text{ ha}^{-1} \text{ mo}^{-1}$ at Ecoregions 56h and 56b, respectively.

Our results also suggest that a total forest loss of ~680 ha due to the conversion to cropland and urban (i.e., the main cover type classes within the watershed) during 2001–2016 led to seasonal and monthly cooling effects at the watershed scale that, on average, were equivalent to $\sim -179 \text{ Mg C}_{\text{eq}} \text{ gs}^{-1}$ and $\sim -374 \text{ Mg C}_{\text{eq}} \text{ mo}^{-1}$, respectively.

These amounts equal approximately 90 ha and 190 ha, respectively, of mature forest net carbon sequestration in the same region, assuming an average value of $2 \text{ Mg C ha}^{-1} \text{ yr}^{-1}$.

4.4. Seasonal Percent Contributions to the Total Cooling and Warming

In line with other studies [55], the largest contribution to the overall total seasonal $\text{GWI}_{\Delta\alpha}$ came from the non-growing season months, during which all the cover types exhibited cooling effects that varied in magnitude depending on the ecoregion. Once again, urban was the only cover type that contributed to warming effects in the growing season, generally following a decreasing trend going from June to September. Such results echo the need reported in previous work to advance research on the importance of surface albedo modification within urban components (e.g., pavements, roofs, walls) as climate regulation strategy to resolve the urban energy budget and energy demand [38,56]. However, it should be noted that urban areas are composed of infrastructure (e.g., roofs, walls, pavements, etc.) and other cover types (e.g., trees, grasses, bare soil, water bodies, etc.) with varying albedo contributions, which were not considered in this study (see next section for more details). Nevertheless, the seasonal analysis clearly confirmed that the contributions to the total landscape cooling or warming effect varied by ecoregion. We found that albedo climate benefits either contributed net cooling/warming or a net neutral effect of the at landscape scale depending on the ecoregion.

4.5. Assumptions and Limitations of the Study

Several assumptions and limitations in our study could benefit computations of albedo-induced global warming impact ($\text{GWI}_{\Delta\alpha}$) elsewhere. The first assumption is related to the choice of the time horizon (TH, see Equation (4)) fixed at a 100-year period. The choice of either short or long time horizons can either over- or de-accentuate $\text{GWI}_{\Delta\alpha}$ values [57]. Specifically, by keeping TH fixed at 100 years, we assume that the land cover composition of the study area will remain the same for the next 100 years, although it is likely that the land cover over the next 100 years will be very different. However, by setting $\text{TH} = 100$, we aligned our study with the Kyoto Protocol [11,44], and hence with the IPCC protocols.

There is also uncertainty associated with the datasets employed in this study. For example, the MODIS MCD43 albedo product has a pixel with a nominal spatial resolution of $500 \times 500 \text{ m}$, which has been shown not to properly match the effective spatial resolution (usually much higher than the nominal one [58,59]). However, previous attempts by researchers to analyze the effective spatial resolution of the MODIS albedo product [60,61] were limited to a single homogeneous area. For areas characterized by substantial land surface heterogeneity, similar to the one presented in this work, the effective spatial representativeness of the pixel is hard to determine [58]. Regarding land cover classification assumptions, we acknowledge that NLCD data are not annually available like albedo data. To overcome this limitation, when NLCD data were not available for a particular year, we assumed land cover was similar to the previous year available. Although the inter-annual LULCC for those years may not be captured, in this way, we were able to carry on a longer timeseries analysis of albedo which otherwise would have been limited to only 7 years (i.e., 2001, 2004, 2006, 2008, 2011, 2013, and 2016). A second assumption regards our analysis of urban areas. The NLCD provides four sub-classes of impervious surfaces (i.e., <20%, between 20% and 49%, between 50% and 79%, and between 80% and 100% of the total cover) composing the developed (i.e., urban) class. However, in this study, we aggregated the four sub-classes into one single “urban” land cover class. We are aware that by doing so, we may have obtained less than precise values of albedo change in urban areas. Other studies [62] have demonstrated that urban heat island intensity (UHII) is highly sensitive to the spatial context of urban areas (i.e., urban, rural, and their combination). Despite this, the focus of our study was not to investigate the importance of urban albedo modifications in the context of UHII effects. We acknowledge that a clear definition of urban and rural contexts would benefit future investigations of albedo changes in urban areas.

We investigated the contribution of landscape composition due to land transformation on $\text{GWI}_{\Delta\alpha}$ in the context of climate change mitigations by considering the forest cover type as the reference for the entire study area [24]. However, without other references, our calculations cannot estimate the forests' contribution to $\text{GWI}_{\Delta\alpha}$. This hinders a comprehensive synthesis of the total climate emission or mitigation of the watershed, considering that the low albedo of forests contributes to climate warming [63]. Moreover, regarding indirect biophysical effects, forests' role in mitigating climate change is multifaceted. Recent studies have demonstrated how re-/afforestation strategies can increase low-level cloud cover formation, which, depending on the forest type, results in cooling effects [64]. Analyzing land transformation with reference to forests is only one method. For example, other studies and policymakers have focused on land transformation in the context of bioenergy conversions [55] and land management practices to compare landscape dynamics to agriculture [65–67].

We also acknowledge that the instantaneous albedo values at 10:30 a.m. local time are likely different from the daily averages. In this study, we utilized albedo estimated by the MODIS BRDF function, which is the composite of a 16-day period [68], with albedo values from a single snapshot at 10:30 a.m. local time (e.g., MODIS Terra morning overpassing time). However, there is increasing evidence showing diurnal variations of albedo [68,69] under different sky conditions. Nevertheless, the MODIS MCD43 albedo product is soundly validated [70–72], as well as widely accepted for retrieving albedo from other remote sensing products [32,73–77] and presenting overall good accuracy compared to in situ daily averages [70].

Lastly, we considered the growing season and monthly albedo at 10:30 a.m. local time by computing the median composite (see Appendix A.1), which prevented us from accounting for the effects of land surface characteristics (i.e., vegetation properties, such as leaf area index, and landscape heterogeneity) on the spatiotemporal variation of albedo among and within patches of the same type. This represents a limitation, as during the growing season, vegetation cover and canopy structure and albedo are negatively correlated due to the varying capacity of the canopy to absorb incoming solar radiation [78]. Our cover type categories did not reflect these differences, so future efforts will be needed to quantify such differences, including the use of other remote sensing metrics and instantaneous measurements [79].

5. Conclusions

Albedo-induced global warming impact ($\text{GWI}_{\Delta\alpha}$) accounted for significant climate benefits (i.e., C_{eq} mitigation) due to land cover changes and structural variations across the landscape. Looking at individual cover types, the climate benefits were higher in cropland, with seasonal and monthly offsets of 18% and 83%, respectively, of the annual greenhouse gas emissions of maize fields in the same area. The second-highest benefits were found in pasture lands. However, urban showed near-neutral albedo climate benefits. Notably, the overall change in landscape composition within the five ecoregions caused different net landscape C_{eq} mitigations. Seasonal climate benefits ranged from $-6.89 \text{ Mg } C_{\text{eq}} \text{ ha}^{-1} \text{ gs}^{-1}$ at Ecoregion 56d to $-11.36 \text{ Mg } C_{\text{eq}} \text{ ha}^{-1} \text{ gs}^{-1}$ at Ecoregion 56b, and monthly climate benefits ranged from $-9.14 \text{ Mg } C_{\text{eq}} \text{ ha}^{-1} \text{ mo}^{-1}$ at Ecoregion 56h to $-14.89 \text{ Mg } C_{\text{eq}} \text{ ha}^{-1} \text{ mo}^{-1}$ at Ecoregion 56b. Changes in albedo due to land cover changes and landscape composition are of fundamental importance in the context of landscape climate regulation. We must couple these estimates with biogeochemical (i.e., GHGs) climate benefits to increase our understanding of the magnitude that various human-induced mechanisms contribute to climate change.

Supplementary Materials: The following supporting information can be downloaded at: <https://www.mdpi.com/article/10.3390/land11020283/s1>, Table S1: Downscaling model; Table S2: Seasonal and monthly albedo; Tables S3.1–3.5: Growing season albedo-induced GWI at ecoregions; Tables S4.1–4.5: Monthly albedo-induced GWI at ecoregions; Table S5: ANOVA model; Table S6: GWI contributions; Table S7: GWI contributions higher than average; Tables S8.1–8.5: Growing season albedo-induced RF at ecoregions; Tables S9.1–9.5: Monthly albedo-induced RF at ecoregions; Figure S1: Albedo-induced RF.

Author Contributions: Conceptualization, P.S. and J.C.; Data curation, P.S. and V.G.; Formal analysis, P.S., V.G., M.A. and C.L.; Funding acquisition, J.C. and G.P.R.; Investigation, J.C.; Methodology, P.S., V.G., M.A., C.L., G.S. and J.Y.; Supervision, J.C., M.A. and G.P.R.; Writing—original draft, P.S.; Writing—review & editing, P.S., J.C., V.G., M.A., C.L., G.S., J.Y. and G.P.R. All authors have read and agreed to the published version of the manuscript.

Funding: This study was supported by the NASA Carbon Cycle & Ecosystems program (NNX17AE16G), the Great Lakes Bioenergy Research Center funded by the U.S. Department of Energy, Office of Science, Office of Biological (DE-SC0018409) and Environmental Research (DE-FC02-07ER64494), and the Natural Science Foundation Long-term Ecological Research Program (DEB 1637653) at the Kellogg Biological Station.

Institutional Review Board Statement: Not applicable.

Informed Consent Statement: Not applicable.

Data Availability Statement: The data presented in this study are available on request from the author.

Acknowledgments: We thank Maowei Liang for helpful suggestions with statistical analyses, and Kristine Blakeslee and Jane Schuette for helpful edits and comments. The NASA POWER datasets were obtained from the NASA Langley Research Center POWER Project funded through the NASA Earth Science Directorate Applied Science Program. We also thank the two anonymous reviewers who helped to improve the quality of our manuscript.

Conflicts of Interest: The authors declare no conflict of interest.

Appendix A. Materials and Methods

Appendix A.1. Google Earth Engine Processing

Instantaneous albedo data at 10:30 a.m. local time (MODIS Terra morning overpassing time) from the MODIS Bidirectional Reflectance Distribution Function (BRDF) MCD43A3 (v006) product [31] was produced by the inversion of a BRDF model against a 16-day moving window of MODIS observations at 500×500 m spatial resolution. For each image, we selected the “Albedo_WSA_shortwave” (i.e., white-sky albedo) band and rescaled it to 0–1. For quality control, we applied the quality band “BRDF_Albedo_Band_Mandatory_Quality_shortwave” (i.e., the full BRDF inversion) [11,80] by filtering out pixels not meeting the control protocols. We then used an additional quality band (“Snow_BRDF_Albedo”) from the MCD43A2 product [81] to further filter and select quality snow-albedo retrievals in the MCD43A3 product. To obtain the growing season at watershed level for each year, we applied the same methodology as Jeong et al. [33] and Sciusco et al. [11]. Briefly, we used the enhanced vegetation index (EVI) to identify the growing season by detecting the EVI inflection points (i.e., the dates) when maximum and minimum change rate in greenness occurred over the entire watershed. We obtained 16-day composite time series of EVI at a 250×250 m spatial resolution from the most recent collection (V006) of the MODIS MYD13Q1 product [82]. Similar to the quality control protocols for albedo product, we filtered and selected only good quality EVI pixels by applying the quality band “SummaryQA” from the MYD13Q1 product. Both albedo and EVI acquisitions referred to approximately 10:30 a.m. and 1:00 p.m. local time, respectively, when MODIS (Terra and Aqua, respectively) passes over the study area. Lastly, we created median composite of the albedo data into growing season (i.e., roughly from March–November for the 19-year period) and monthly (i.e., January–December, over the 19-year period, less March, which we removed because few images were available and likely due to high cloud cover) time-steps at 10:30 a.m. local time.

Appendix A.2. Clearness Index (K_T) for Calculation of Albedo-Induced Radiative Forcing at the Top-of-Atmosphere ($RF_{\Delta\alpha}$)

Instantaneous albedo-induced radiative forcing at the top-of-atmosphere ($RF_{\Delta\alpha}$; see Equation (3)) using the solar radiation at the Earth's surface is calculated [37,38] as:

$$RF_{\Delta\alpha} = -(SW_{TOA} \cdot \Delta\alpha_p) \quad (A1)$$

where SW_{TOA} is the incident shortwave radiation at the top-of-atmosphere and $\Delta\alpha_p$ is the change in planetary albedo. Changes in planetary albedo ($\Delta\alpha_p$) are linearly related to changes in surface albedo ($\Delta\alpha_s$) as follows [37,42,83,84]:

$$\Delta\alpha_p = f_a \cdot \Delta\alpha_s \quad (A2)$$

where f_a is a two-way atmospheric transmittance parameter that accounts for both the reflection and absorption of solar radiation through the atmosphere, and it can be decomposed into downward and upward transmittance coefficients as follows [83]:

$$f_a = K_T \cdot T_a \quad (A3)$$

where the clearness index K_T is the fraction of SW_{TOA} reaching the Earth's surface, T_a is the upward atmospheric transmittance factor (i.e., the fraction of the radiation reflected by the Earth's surface back at the top-of-atmosphere). In turn, T_a is calculated as:

$$T_a = \frac{SW_{in}}{SW_{TOA}} \quad (A4)$$

where SW_{in} and SW_{TOA} are the incident shortwave radiation at the surface and at the top-of-atmosphere, respectively. By replacing Equations (A2)–(A4) in (A1), we obtain Equation (3), which is reproduced here for the reader's convenience:

$$RF_{\Delta\alpha} = -(SW_{in} \cdot K_T \cdot \Delta\alpha_s) \quad (A5)$$

where $RF_{\Delta\alpha}$ ($W\ m^{-2}$) is the instantaneous albedo-induced radiative forcing at the top-of-atmosphere at 10:30 a.m. local time, SW_{in} , K_T , and $\Delta\alpha_{si}$ are the incident shortwave radiation at the surface, the clearness index, and the surface albedo difference between a cover type i and the reference forest for growing season and monthly periods and for each ecoregion (see Equation (2)).

We also calculated $RF_{\Delta\alpha}$ by using the upward atmospheric transmittance factor (T_a ; Equation (A4)) as in Carrer et al. [13] and Sciusco et al. [11], although the differences in $RF_{\Delta\alpha}$ calculated with the use of K_T and T_a were negligible, so we decided to only report $RF_{\Delta\alpha}$ calculated with K_T .

Appendix A.3. Carbon-Dioxide Airborne Fraction ($AF(t)$)

The carbon-dioxide (CO_2) airborne fraction that remains in the atmosphere at time (t) following a single pulse emission is modeled with an exponential function through multi-model impulse response function analysis [40] as follows:

$$AF(t) = a_0 + \sum_{i=1}^3 \left[a_i e^{\frac{-t}{\tau_i}} \right] \quad (A6)$$

where t represents the time in years, a_i and τ_i are the fitted coefficients representing the decay of CO_2 pulse emission in the atmosphere over time. The recommended mean coefficients obtained from the multi-model impulse response function analysis are: $a_0 = 0.2173$ (the fraction of CO_2 that remains permanently in the atmosphere); $a_1 = 0.2240$; $a_2 = 0.2824$; $a_3 = 0.2763$; $\tau_1 = 394.4$; $\tau_2 = 36.54$; and $\tau_3 = 4.304$ [40].

Appendix A.4. Analysis of Variance (ANOVA)

Prior to running the analysis of variance (ANOVA) (Equations (5) and (6)), we checked for normal distribution of the residuals (i.e., normality and heteroscedasticity assumptions) and outliers, and performed the Mauchly's test (i.e., sphericity assumption) when necessary. Wherever the sphericity assumption was violated, we applied the Greenhouse-Geisser corrections. We then calculated the generalized eta-squared (η^2) [85] to examine the variance of dependent variable $\text{GWI}_{\Delta\alpha}$ by ecoregion, cover type and their interactions. Lastly, we carried out a post-hoc Tukey test analysis to see whether differences in the least square means (LSMs) of $\text{GWI}_{\Delta\alpha}$ among and within cover type and ecoregions were significant. All analyses were carried out in RStudio v. 1.2.5033 [35], using the R-packages "ez", "nlme", "lsmeans", and "multcomp" [86–89].

References

1. Myhre, G.; Shindell, D.; Pongratz, J. Anthropogenic and natural radiative forcing. In *Climate Change 2013: The Physical Science Basis. Working Group I Contribution to the Fifth Assessment Report of the Intergovernmental Panel on Climate Change*; Stocker, T.F., Ed.; Cambridge University Press: Cambridge, UK; New York, NY, USA, 2014; pp. 659–740; ISBN 978-1-107-41532-4.
2. Hollinger, D.Y.; Ollinger, S.V.; Richardson, A.D.; Meyers, T.P.; Dail, D.B.; Martin, M.E.; Scott, N.A.; Arkebauer, T.J.; Baldocchi, D.D.; Clark, K.L.; et al. Albedo estimates for land surface models and support for a new paradigm based on foliage nitrogen concentration. *Glob. Change. Biol.* **2010**, *16*, 696–710. [[CrossRef](#)]
3. Vitousek, P.M.; Mooney, H.A.; Lubchenco, J.; Melillo, J.M. Human domination of Earth's ecosystems. *Science* **1997**, *277*, 7. [[CrossRef](#)]
4. Wackernagel, M.; Schulz, N.B.; Deumling, D.; Linares, A.C.; Jenkins, M.; Kapos, V.; Monfreda, C.; Loh, J.; Myers, N.; Norgaard, R.; et al. Tracking the ecological overshoot of the human economy. *Proc. Natl. Acad. Sci. USA* **2002**, *99*, 9266–9271. [[CrossRef](#)] [[PubMed](#)]
5. Kalnay, E.; Cai, M. Impact of urbanization and land-use change on climate. *Nature* **2003**, *423*, 528–531. [[CrossRef](#)] [[PubMed](#)]
6. Pielke, R.A.; Pitman, A.; Niyogi, D.; Mahmood, R.; McAlpine, C.; Hossain, F.; Goldewijk, K.K.; Nair, U.; Betts, R.; Fall, S.; et al. Land use/land cover changes and climate: Modeling analysis and observational evidence. *Wiley Interdiscip. Rev. Clim. Change* **2011**, *2*, 828–850. [[CrossRef](#)]
7. Shao, C.; Li, L.; Dong, G.; Chen, J. Spatial variation of net radiation and its contribution to energy balance closures in grassland ecosystems. *Ecol. Process.* **2014**, *3*, 7. [[CrossRef](#)]
8. Mira, M.; Weiss, M.; Baret, F.; Courault, D.; Hagolle, O.; Gallego-Elvira, B.; Olivos, A. The MODIS (collection V006) BRDF/albedo product MCD43D: Temporal course evaluated over agricultural landscape. *Remote Sens. Environ.* **2015**, *170*, 216–228. [[CrossRef](#)]
9. Stocker, T.F.; Qin, D.; Plattner, G.-K.; Tignor, M.M.B.; Allen, S.K.; Boschung, J.; Nauels, A.; Xia, Y.; Bex, V.; Midgley, P.M. *Climate Change 2013: The Physical Science Basis. Contribution of Working Group I to the Fifth Assessment Report of IPCC the Intergovernmental Panel on Climate Change*; Stocker, T., Qin, D., Plattner, G.-K., Tignor, M., Allen, S., Boschung, J., Nauels, A., Xia, Y., Bex, V., Midgley, P., Eds.; Cambridge University Press: Cambridge, UK; New York, NY, USA, 2014; p. 1535; ISBN 978-1-107-66182-0.
10. Bright, R.M.; Lund, M.T. CO₂-equivalence metrics for surface albedo change based on the radiative forcing concept: A critical review. *Atmospheric Chem. Phys.* **2021**, *21*, 9887–9907. [[CrossRef](#)]
11. Sciusco, P.; Chen, J.; Abraha, M.; Lei, C.; Robertson, G.P.; Laforteza, R.; Shirkey, G.; Ouyang, Z.; Zhang, R.; John, R. Spatiotemporal variations of albedo in managed agricultural landscapes: Inferences to global warming impacts (GWI). *Landsc. Ecol.* **2020**, *35*, 1385–1402. [[CrossRef](#)]
12. Houspanossian, J.; Giménez, R.; Jobbágy, E.; Noretto, M. Surface albedo raise in the south American Chaco: Combined effects of deforestation and agricultural changes. *Agric. For. Meteorol.* **2017**, *232*, 118–127. [[CrossRef](#)]
13. Carrer, D.; Pique, G.; Ferlicoq, M.; Ceamanos, X.; Ceschia, E. What is the potential of cropland albedo management in the fight against global warming? A case study based on the use of cover crops. *Environ. Res. Lett.* **2018**, *13*, 044030. [[CrossRef](#)]
14. Lugato, E.; Cescatti, A.; Jones, A.; Ceccherini, G.; Duveiller, G. Maximising climate mitigation potential by carbon and radiative agricultural land management with cover crops. *Environ. Res. Lett.* **2020**, *15*, 094075. [[CrossRef](#)]
15. Chen, J.; Lei, C.; Sciusco, P. Modeling ecosystem global warming potentials. In *Biophysical Models and Applications in Ecosystem Analysis*; Michigan State University Press: East Lansing, MI, USA, 2021; pp. 119–150; ISBN 978-1-61186-393-2.
16. Gelfand, I.; Sahajpal, R.; Zhang, X.; Izaurreal, R.C.; Gross, K.L.; Robertson, G.P. Sustainable bioenergy production from marginal lands in the US midwest. *Nature* **2013**, *493*, 514–517. [[CrossRef](#)] [[PubMed](#)]
17. Gelfand, I.; Robertson, G.P. Mitigation of greenhouse gas emissions in agricultural ecosystems. In *The Ecology of Agricultural Landscapes: Long-Term Research on the Path to Sustainability*; Oxford University Press: Oxford, UK, 2015; pp. 310–339; ISBN 978-0-19-977348-0.
18. Kauppi, P.; Sedjo, R. Technological and economic potential of options to enhance, maintain, and manage biological carbon reservoirs and geo-engineering. In *Economics of Forestry*; Sedjo, R.A., Ed.; Routledge: London, UK, 2003; pp. 373–416. ISBN 978-1-315-18268-1.
19. Cicerone, R.J. Geoengineering: Encouraging research and overseeing implementation. *Clim. Change.* **2006**, *77*, 221–226. [[CrossRef](#)]
20. Crutzen, P.J. Albedo enhancement by stratospheric sulfur injections: A contribution to resolve a policy dilemma? An editorial essay. In *Paul J. Crutzen: A Pioneer on Atmospheric Chemistry and Climate Change in the Anthropocene*; Crutzen, P.J., Brauch, H.G., Eds.; Springer International Publishing: Cham, Switzerland, 2016; pp. 217–225; ISBN 978-3-319-27460-7.

21. Euskirchen, E.S.; Chen, J.; Li, H.; Gustafson, E.J.; Crow, T.R. Modeling landscape net ecosystem productivity (LandNEP) under alternative management regimes. *Ecol. Model.* **2002**, *154*, 75–91. [[CrossRef](#)]
22. Chen, J.; Brosofske, K.D.; Noormets, A.; Crow, T.R.; Bresee, M.K.; Le Moine, J.M.; Euskirchen, E.S.; Mather, S.V.; Zheng, D. A working framework for quantifying carbon sequestration in disturbed land mosaics. *Environ. Manage.* **2004**, *33*, S210–S221. [[CrossRef](#)]
23. Michigan State Climatologist's Office. *Gull Lake (3504)*; Michigan State University: East Lansing, MI, USA, 2013; Available online: <https://climate.geo.msu.edu/index.html> (accessed on 12 December 2020).
24. Brown, D.G.; Pijanowski, B.C.; Duh, J.D. Modeling the relationships between land use and land cover on private lands in the upper midwest, USA. *J. Environ. Manage.* **2000**, *59*, 247–263. [[CrossRef](#)]
25. Chapman, K.A.; Brewer, R. Prairie and savanna in southern lower Michigan: History, classification, ecology. *Mich. Bot. Club* **2008**, *47*, 48.
26. Schaetzl, R.J.; Darden, J.T.; Brandt, D.S. *Michigan Geography and Geology*; Pearson Custom Publishing: Boston, MA, USA, 2009; p. 696. Available online: <http://catalog.hathitrust.org/api/volumes/oclc/309340740.html> (accessed on 12 December 2020). ISBN 0-536-98716-5.
27. Omernik, J.M.; Griffith, G.E. Ecoregions of the Conterminous United States: Evolution of a hierarchical spatial framework. *Environ. Manage.* **2014**, *54*, 1249–1266. [[CrossRef](#)]
28. United States Environmental Protection Agency. Level III and IV Ecoregions of the Continental United States. Available online: <https://www.epa.gov/eco-research/level-iii-and-iv-ecoregions-continental-united-states> (accessed on 12 December 2020).
29. Yang, L.; Jin, S.; Danielson, P.; Homer, C.; Gass, L.; Bender, S.M.; Case, A.; Costello, C.; Dewitz, J.; Fry, J.; et al. A new generation of the United States National Land Cover Database: Requirements, Research Priorities, Design, and Implementation Strategies. *ISPRS J. Photogramm. Remote Sens.* **2018**, *146*, 108–123. [[CrossRef](#)]
30. Homer, C.; Dewitz, J.; Jin, S.; Xian, G.; Costello, C.; Danielson, P.; Gass, L.; Funk, M.; Wickham, J.; Stehman, S.; et al. Conterminous United States land cover change patterns 2001–2016 from the 2016 National Land Cover Database. *ISPRS J. Photogramm. Remote Sens.* **2020**, *162*, 184–199. [[CrossRef](#)]
31. Land Processes Distributed Active Archive Center MODIS (BRDF) MCD43A3 Albedo Product (v. 6) from 2001–2019. Available online: <https://doi.org/10.5067/MODIS/MCD43A3.006> (accessed on 12 December 2020).
32. Wang, Z.; Schaaf, C.B.; Strahler, A.H.; Chopping, M.J.; Román, M.O.; Shuai, Y.; Woodcock, C.E.; Hollinger, D.Y.; Fitzjarrald, D.R. Evaluation of MODIS albedo product (MCD43A) over grassland, agriculture and forest surface types during dormant and snow-covered periods. *Remote Sens. Environ.* **2014**, *140*, 60–77. [[CrossRef](#)]
33. Jeong, S.-J.; Ho, C.-H.; Gim, H.-J.; Brown, M.E. Phenology shifts at start vs. end of growing season in temperate vegetation over the northern hemisphere for the period 1982–2008. *Glob. Change. Biol.* **2011**, *17*, 2385–2399. [[CrossRef](#)]
34. Gorelick, N.; Hancher, M.; Dixon, M.; Ilyushchenko, S.; Thau, D.; Moore, R. Google Earth Engine: Planetary-scale geospatial analysis for everyone. *Remote Sens. Environ.* **2017**, *202*, 18–27. [[CrossRef](#)]
35. R Core Team. *R: A Language and Environment for Statistical Computing*; R Foundation for Statistical Computing: Vienna, Austria, 2020. Available online: <https://www.R-Project.Org/> (accessed on 12 December 2020).
36. Chen, J.; Sciusco, P.; Ouyang, Z.; Zhang, R.; Henebry, G.M.; John, R.; Roy, D.P. Linear downscaling from MODIS to Landsat: Connecting landscape composition with ecosystem functions. *Landsc. Ecol.* **2019**, *34*, 2917–2934. [[CrossRef](#)]
37. Bright, R.M.; Cherubini, F.; Strømman, A.H. Climate impacts of bioenergy: Inclusion of carbon cycle and albedo dynamics in life cycle impact assessment. *Environ. Impact Assess. Rev.* **2012**, *37*, 2–11. [[CrossRef](#)]
38. Xu, X.; Swei, O.; Xu, L.; Schlosser, C.A.; Gregory, J.; Kirchain, R. Quantifying location-specific impacts of pavement albedo on radiative forcing using an analytical approach. *Environ. Sci. Technol.* **2020**, *54*, 2411–2421. [[CrossRef](#)]
39. Sparks, A. Nasapower: NASA-POWER Data for R. R Package Version 3.0.1. 2020. Available online: <https://CRAN.R-Project.Org/Package=nasapower> (accessed on 12 December 2020).
40. Joos, F.; Roth, R.; Fuglestedt, J.S.; Peters, G.P.; Enting, I.G.; von Bloh, W.; Brovkin, V.; Burke, E.J.; Eby, M.; Edwards, N.R.; et al. Carbon dioxide and climate impulse response functions for the computation of greenhouse gas metrics: A multi-model analysis. *Atmospheric Chem. Phys.* **2013**, *13*, 2793–2825. [[CrossRef](#)]
41. Bright, R.M.; Zhao, K.; Jackson, R.B.; Cherubini, F. Quantifying surface albedo and other direct biogeophysical climate forcings of forestry activities. *Glob. Change. Biol.* **2015**, *21*, 3246–3266. [[CrossRef](#)]
42. Muñoz, I.; Campa, P.; Fernández-Alba, A.R. Including CO₂-emission equivalence of changes in land surface albedo in life cycle assessment. Methodology and case study on greenhouse agriculture. *Int. J. Life Cycle Assess.* **2010**, *15*, 672–681. [[CrossRef](#)]
43. Kaye, J.P.; Quemada, M. Using cover crops to mitigate and adapt to climate change: A review. *Agron. Sustain. Dev.* **2017**, *37*, 4. [[CrossRef](#)]
44. Boucher, O.; Friedlingstein, P.; Collins, B.; Shine, K.P. The indirect global warming potential and global temperature change potential due to methane oxidation. *Environ. Res. Lett.* **2009**, *4*, 044007. [[CrossRef](#)]
45. Li, Q.; Ma, M.; Wu, X.; Yang, H. Snow cover and vegetation-induced decrease in global albedo from 2002 to 2016. *J. Geophys. Res. Atmos.* **2018**, *123*, 124–138. [[CrossRef](#)]
46. Abraha, M.; Gelfand, I.; Hamilton, S.K.; Chen, J.; Robertson, G.P. Carbon debt of field-scale conservation reserve program grasslands converted to annual and perennial bioenergy crops. *Environ. Res. Lett.* **2019**, *14*, 024019. [[CrossRef](#)]
47. Robertson, G.P. Greenhouse gases in intensive agriculture: Contributions of individual gases to the radiative forcing of the atmosphere. *Science* **2000**, *289*, 1922–1925. [[CrossRef](#)]
48. Hammerle, A.; Haslwanter, A.; Tappeiner, U.; Cernusca, A.; Wohlfahrt, G. Leaf area controls on energy partitioning of a mountain grassland. *Biogeosci. Discuss.* **2007**, *4*, 3607–3638. [[CrossRef](#)]

49. Rechid, D.; Raddatz, T.J.; Jacob, D. Parameterization of snow-free land surface albedo as a function of vegetation phenology based on MODIS data and applied in climate modelling. *Theor. Appl. Climatol.* **2009**, *95*, 245–255. [[CrossRef](#)]
50. Lukeš, P.; Rautiainen, M.; Manninen, T.; Stenberg, P.; Möttöus, M. Geographical gradients in boreal forest albedo and structure in Finland. *Remote Sens. Environ.* **2014**, *152*, 526–535. [[CrossRef](#)]
51. Kuusinen, N.; Stenberg, P.; Korhonen, L.; Rautiainen, M.; Tomppo, E. Structural factors driving boreal forest albedo in Finland. *Remote Sens. Environ.* **2016**, *175*, 43–51. [[CrossRef](#)]
52. Zheng, L.; Zhao, G.; Dong, J.; Ge, Q.; Tao, J.; Zhang, X.; Qi, Y.; Doughty, R.B.; Xiao, X. Spatial, temporal, and spectral variations in albedo due to vegetation changes in China's grasslands. *ISPRS J. Photogramm. Remote Sens.* **2019**, *152*, 1–12. [[CrossRef](#)]
53. Curtis, P.S.; Hanson, P.J.; Bolstad, P.; Barford, C.; Randolph, J.C.; Schmid, H.P.; Wilson, K.B. Biometric and eddy-covariance based estimates of annual carbon storage in five eastern north American deciduous forests. *Agric. For. Meteorol.* **2002**, *113*, 3–19. [[CrossRef](#)]
54. Welsh, W.F.; Brown, D.G.; Messina, J.P. Land use and cover. In *Michigan Geography and Geology*; Schaetzl, R.J., Darden, J.T., Brandt, D., Eds.; Pearson Custom Publishing: Boston, MA, USA, 2009; pp. 446–457; ISBN 0-536-98716-5.
55. Abraha, M.; Chen, J.; Hamilton, S.K.; Sciusco, P.; Lei, C.; Shirkey, G.; Yuan, J.; Robertson, G.P. Albedo-induced global warming impact of conservation reserve program grasslands converted to annual and perennial bioenergy crops. *Environ. Res. Lett.* **2021**, *16*, 084059. [[CrossRef](#)]
56. Jandaghian, Z.; Akbari, H. The effect of increasing surface albedo on urban climate and air quality: A detailed study for Sacramento, Houston, and Chicago. *Climate* **2018**, *6*, 19. [[CrossRef](#)]
57. Anderson-Teixeira, K.J.; Snyder, P.K.; Twine, T.E.; Cuadra, S.V.; Costa, M.H.; de Lucia, E.H. Climate-regulation services of natural and agricultural ecoregions of the Americas. *Nat. Clim. Change.* **2012**, *2*, 177–181. [[CrossRef](#)]
58. Zhou, H.; Liang, S.; He, T.; Wang, J.; Bo, Y.; Wang, D. Evaluating the spatial representativeness of the MODerate Resolution Image Spectroradiometer albedo product (MCD43) at AmeriFlux sites. *Remote Sens.* **2019**, *11*, 547. [[CrossRef](#)]
59. Moreno-Ruiz, J.A.; García-Lázaro, J.R.; Arbelo, M.; Riaño, D. A comparison of burned area time series in the Alaskan boreal forests from different remote sensing products. *Forests* **2019**, *10*, 363. [[CrossRef](#)]
60. Campagnolo, M.L.; Sun, Q.; Liu, Y.; Schaaf, C.; Wang, Z.; Román, M.O. Estimating the effective spatial resolution of the operational BRDF, albedo, and nadir reflectance products from MODIS and VIIRS. *Remote Sens. Environ.* **2016**, *175*, 52–64. [[CrossRef](#)]
61. Hovi, A.; Lindberg, E.; Lang, M.; Arumäe, T.; Peuhkurinen, J.; Sirparanta, S.; Pyankov, S.; Rautiainen, M. Seasonal Dynamics of albedo across European boreal forests: Analysis of MODIS albedo and structural metrics from airborne LiDAR. *Remote Sens. Environ.* **2019**, *224*, 365–381. [[CrossRef](#)]
62. Zhao, Z.; Sharifi, A.; Dong, X.; Shen, L.; He, B.-J. Spatial variability and temporal heterogeneity of surface urban heat island patterns and the suitability of local climate zones for land surface temperature characterization. *Remote Sens.* **2021**, *13*, 4338. [[CrossRef](#)]
63. Bonan, G.B. Forests and climate change: Forcings, feedbacks, and the climate benefits of forests. *Science* **2008**, *320*, 1444–1449. [[CrossRef](#)]
64. Duveiller, G.; Filipponi, F.; Ceglar, A.; Bojanowski, J.; Alkama, R.; Cescatti, A. Revealing the widespread potential of forests to increase low level cloud cover. *Nat. Commun.* **2021**, *12*, 4337. [[CrossRef](#)] [[PubMed](#)]
65. Davin, E.L.; Seneviratne, S.I.; Ciais, P.; Ollio, A.; Wang, T. Preferential cooling of hot extremes from cropland albedo management. *Proc. Natl. Acad. Sci. USA* **2014**, *111*, 9757–9761. [[CrossRef](#)]
66. Cai, H.; Wang, J.; Feng, Y.; Wang, M.; Qin, Z.; Dunn, J.B. Consideration of land use change-induced surface albedo effects in life-cycle analysis of biofuels. *Energy Environ. Sci.* **2016**, *9*, 2855–2867. [[CrossRef](#)]
67. Sieber, P.; Ericsson, N.; Hammar, T.; Hansson, P.-A. Including albedo in time-dependent LCA of bioenergy. *GCB Bioenergy* **2020**, *12*, 410–425. [[CrossRef](#)]
68. He, T.; Wang, D.; Qu, Y. Land surface albedo. In *Comprehensive Remote Sensing*; Elsevier: Amsterdam, The Netherlands, 2018; pp. 140–162. ISBN 978-0-12-803221-3.
69. Wang, D.; Liang, S.; He, T.; Yu, Y.; Schaaf, C.; Wang, Z. Estimating daily mean land surface albedo from MODIS data. *J. Geophys. Res. Atmos.* **2015**, *120*, 4825–4841. [[CrossRef](#)]
70. Wang, Z.; Schaaf, C.B.; Chopping, M.J.; Strahler, A.H.; Wang, J.; Román, M.O.; Rocha, A.V.; Woodcock, C.E.; Shuai, Y. Evaluation of Moderate-resolution Imaging Spectroradiometer (MODIS) snow albedo product (MCD43A) over tundra. *Remote Sens. Environ.* **2012**, *117*, 264–280. [[CrossRef](#)]
71. Qu, Y.; Liu, Q.; Liang, S.; Wang, L.; Liu, N.; Liu, S. Direct-estimation algorithm for mapping daily land-surface broadband albedo from MODIS data. *IEEE Trans. Geosci. Remote Sens.* **2014**, *52*, 907–919. [[CrossRef](#)]
72. Corbea-Pérez, A.; Calleja, J.F.; Recondo, C.; Fernández, S. Evaluation of the MODIS (C6) daily albedo products for Livingston Island, Antarctic. *Remote Sens.* **2021**, *13*, 2357. [[CrossRef](#)]
73. Stroeve, J.; Box, J.E.; Gao, F.; Liang, S.; Nolin, A.; Schaaf, C. Accuracy assessment of the MODIS 16-day albedo product for snow: Comparisons with Greenland in situ measurements. *Remote Sens. Environ.* **2005**, *94*, 46–60. [[CrossRef](#)]
74. Liu, J.; Schaaf, C.; Strahler, A.; Jiao, Z.; Shuai, Y.; Zhang, Q.; Roman, M.; Augustine, J.A.; Dutton, E.G. Validation of Moderate resolution Imaging Spectroradiometer (MODIS) albedo retrieval algorithm: Dependence of albedo on solar zenith angle. *J. Geophys. Res. Atmos.* **2009**, *114*, 114. [[CrossRef](#)]
75. Cescatti, A.; Marcolla, B.; Vannan, S.K.S.; Pan, J.Y.; Román, M.O.; Yang, X.; Ciais, P.; Cook, R.B.; Law, B.E.; Matteucci, G.; et al. Intercomparison of MODIS albedo retrievals and in situ measurements across the global FLUXNET network. *Remote Sens. Environ.* **2012**, *121*, 323–334. [[CrossRef](#)]

76. He, T.; Liang, S.; Wang, D.; Wu, H.; Yu, Y.; Wang, J. Estimation of surface albedo and directional reflectance from Moderate resolution Imaging Spectroradiometer (MODIS) observations. *Remote Sens. Environ.* **2012**, *119*, 286–300. [[CrossRef](#)]
77. Roman, M.O.; Gatebe, C.K.; Shuai, Y.; Wang, Z.; Gao, F.; Masek, J.G.; He, T.; Liang, S.; Schaaf, C.B. Use of in situ and airborne multiangle data to assess MODIS- and Landsat-based estimates of directional reflectance and albedo. *IEEE Trans. Geosci. Remote Sens.* **2013**, *51*, 1393–1404. [[CrossRef](#)]
78. Tian, L.; Chen, J.; Shao, C. Interdependent dynamics of LAI-albedo across the roofing landscapes: Mongolian and Tibetan Plateaus. *Remote Sens.* **2018**, *10*, 1159. [[CrossRef](#)]
79. Giannico, V.; Chen, J.; Shao, C.; Ouyang, Z.; John, R.; Laforteza, R. Contributions of landscape heterogeneity within the footprint of eddy-covariance towers to flux measurements. *Agric. For. Meteorol.* **2018**, *260–261*, 144–153. [[CrossRef](#)]
80. Chrysoulakis, N.; Mitraka, Z.; Gorelick, N. Exploiting satellite observations for global surface albedo trends monitoring. *Theor. Appl. Climatol.* **2018**. [[CrossRef](#)]
81. Land Processes Distributed Active Archive Center MODIS (BRDF) MCD43A2 Albedo Quality Dataset (v. 6) from 2001–2019. Available online: <https://doi.org/10.5067/MODIS/MCD43A2.006> (accessed on 12 December 2020).
82. Land Processes Distributed Active Archive Center MODIS MYD13Q1 Vegetation Indices Product (v. 6) from 2001–2019. Available online: <https://doi.org/10.5067/MODIS/MYD13Q1.006> (accessed on 12 December 2020).
83. Lenton, T.M.; Vaughan, N.E. The radiative forcing potential of different climate geoengineering options. *Atmos Chem Phys.* **2009**, *9*, 5539–5561. [[CrossRef](#)]
84. Cherubini, F.; Bright, R.M.; Strømman, A.H. Site-specific global warming potentials of biogenic CO₂ for bioenergy: Contributions from carbon fluxes and albedo dynamics. *Environ. Res. Lett.* **2012**, *7*, 045902. [[CrossRef](#)]
85. Bakeman, R. Recommended effect size statistics for repeated measures designs. *Behav. Res. Methods* **2005**, *37*, 379–384. [[CrossRef](#)]
86. Lawrence, M.A. Ez: Easy Analysis and Visualization of Factorial Experiments. 2016. Available online: <https://CRAN.R-project.org/package=eaz> (accessed on 12 December 2020).
87. Pinheiro, J.; Douglas, B.; Saikat, D.R.; Deepayan, S.; Siem, H.; Bert, V.W. R-Core nlme: Linear and Nonlinear Mixed Effects Models. 2017. Available online: <https://CRAN.R-project.org/package=nlme> (accessed on 12 December 2020).
88. Lenth, R. Lsmmeans: Least-Squares Means. 2018. Available online: <https://CRAN.R-project.org/package=lsmmeans> (accessed on 12 December 2020).
89. Hothorn, T.; Bretz, F.; Westfall, P.; Heiberger, R.M.; Schuetzenmeister, A.; Scheibe, S. Multcomp: Simultaneous Inference in General Parametric Models. 2020. Available online: <https://CRAN.R-project.org/package=multcomp> (accessed on 12 December 2020).